Acoustic Holography and Holophony, Laboratory
Lecture-Number: 17.0000

Measurement of a variably curved Line-Source and Analysis of its Circular Radiation Pattern

Alexander Mülleder, 01531717
Nico Seddiki, 01126098
Leon Merkel, 11745386

Lecturer:

Ass.Prof. DI. Dr.rer.nat. Franz Zotter

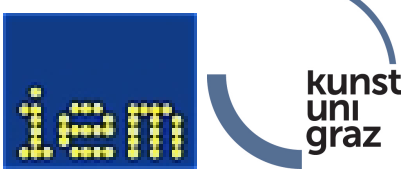

Institute for Electronic Music and Acoustics
University of Music and Performing Arts
December 14, 2023

Contents

1 Introduction

This report investigates the circular radiation pattern of a variable curved line source, measured during the laboratory *„Acoustic Holography and Holophony“*. The 3D-printed small-size variable curved line source, designed by Lukas Gölles and fabricated by the Institute of Electronic Music and Acoustics, was chosen as the device under test. The line array (LA) consists of eight single loudspeaker enclosures, measured in four configurations. The different curvatures aim for coverage designs with specific distance-dependent sound pressure level (SPL) descents. In nearly anechoic conditions for high frequencies, the individual loudspeakers of the LA are measured with 10° spatial resolution in the azimuth and zenith orientation, respectively. The measurement at a medial radius of 0.75 m corresponded to a near-field sampling. Subsequently, the spatial resolution was increased by interpolating with circular harmonics, and the near-field results were geometrically extrapolated to the far field to investigate the SPL decay per distance.

2 Methods & Experimental Setup

2.1 System Identification

Any electrical or acoustical time-invariant system can be determined by its excitation response with a Dirac unit pulse $\delta[n]$. This response is called the impulse response (IR). Therefore, measuring IRs is a common task in audio signal processing. As a perfect Dirac unit pulse can not be perfectly reproduced with a loudspeaker, the exponential sweep (ES) is used as an excitation signal in the current work due to several advantages. The ES is gainful because of its low crest factor and the possibility of suppressing any harmonic distortion. [MBL07].

2.1.1 Impulse Response

In order to measure the IR of any linear time-invariant system, an excitation signal $x[n]$ is generated in such a way that the signal $x_{\text{inv}}[n]$ can be easily determined by inverting the signal. According to [HCZ09], convolution of the inverted signal and the signal itself leads to a potentially scaled by a factor C and time-shifted unit pulse $\delta[n_0 - n]$, such that

$$\sum_{l=0}^{N-1} x[l]\, x_{\text{inv}}[n-l] = C\, \delta[n_0 - n]\,. \tag{2.1}$$

The convolution of the measured signal $y[n]$ and the inverse of the excitation signal will give the scaled and time-shifted impulse response $h[n]$,

$$C\, h[n_0 - n] = \sum_{l=0}^{N-1} y[l]\, x_{\text{inv}}[n-l]\,. \tag{2.2}$$

The IR can also be derived in the frequency domain using the Fourier transformation (FT), where the convolution becomes multiplication. Applying the FT ($\mathcal{F}$) to the signals and obtaining $h[n]$ by calculating the inverse FT ($\mathcal{F}^{-1}$) as

$$h[n] = \mathcal{F}^{-1}\left\{\frac{\mathcal{F}\{y[n]\}}{\mathcal{F}\{x[n]\}}\right\}\,. \tag{2.3}$$

2.1.2 Exponential Sweep

In order to derive the exponential sweep (ES), a basic discrete sinus signal can be described as

$$x[n] = \sin(\phi[n]) \quad , \quad \phi[n] = \int_0^{N-1} \omega[n]\mathrm{d}n\,, \tag{2.4}$$

where $\phi[n]$ is the current phase value and N the number of samples. A sinus sweep with exponentially increasing frequency can be derived using the general exponential ansatz for $\omega[n]$

$$\omega[n] = ce^{bn}\,. \tag{2.5}$$

By evaluating the exponential ansatz, from eq. (2.5), with respect to the starting frequency ω_0 and the end frequency ω_1 yields to the phase $\phi[n]$ with its constants c and b

$$c = \omega_0 \quad , \quad b = \frac{1}{N-1} \ln\left(\frac{\omega_1}{\omega_0}\right) . \tag{2.6}$$

Therefore, $x[n]$ can be calculated by evaluating the sinusiod with the phase $\varphi[n]$ that starts with 0 as

$$x[n] = \sin\left[\frac{c}{b}\left(e^{b \cdot n} - 1\right)\right] . \tag{2.7}$$

In order to also end the exponential sweep with zero phase, an optimal starting frequency was calculated as presented in [ZG22]. By having an exemplary $f_s = 48\,\text{kHz}$ and a sweep length of $N = 96000$ samples, a starting frequency of $f_0 = 19.993\,\text{Hz}$ is calculated. The resulting normalized sweep in frequency/time representation and the convolution with its inverse are depicted in Fig. 2.1 and Fig. 2.2.

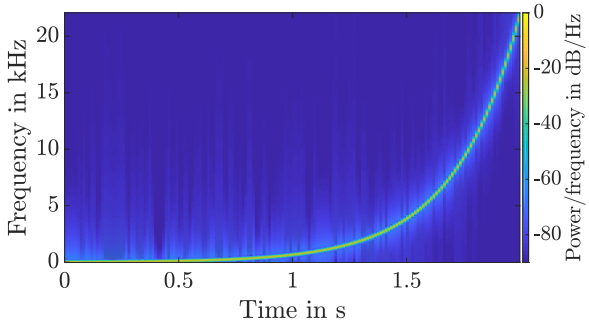

Figure 2.1: exponential sweep

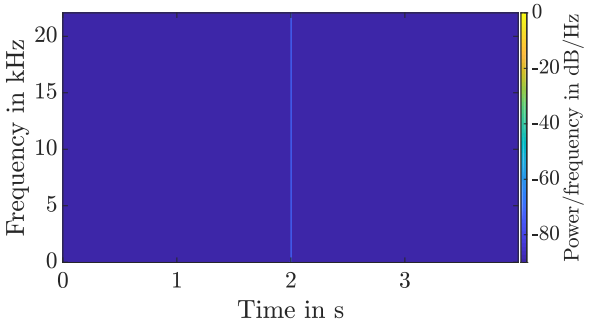

Figure 2.2: convolution of $x[n]$ and $x_{\text{inv}}[n]$

2.2 Experimental Setup

Four different LA designs were investigated, where configuration (1) aims for a decay of 0 dB per doubling of the distance (dod). Configurations (2) and (3) are designed for 1.5 dB and 3 dB per dod. The last configuration (4) was just a straight array. The exact design angles are shown in Tab. 2.1.

Enclosure number (From top to bottom)	Config. (1) (0dB/dod)	Config. (2) (-1.5dB/dod)	Config. (3) (-3dB/dod)	Config. (4) Straight Array
Array tilt angle	6.1°	6.1°	6.1°	6.1°
1	0°	0°	0°	0°
2	0°	0°	1°	0°
3	0°	1°	1°	0°
4	0°	0°	1°	0°
5	1°	1°	1°	0°
6	1°	1°	2°	0°
7	2°	3°	2°	0°
8	10°	6°	3°	0°
Accumulated	**20.1°**	**18.1°**	**17.1°**	**6.1°**

Table 2.1: Design angles of the three configurations

For the measurement, 18 equally spaced *NTI M2230* pressure microphones were mounted on a fixed arc-shaped suspension, resulting in observation angles from $5° - 175°$ in $10°$ steps at a radius of

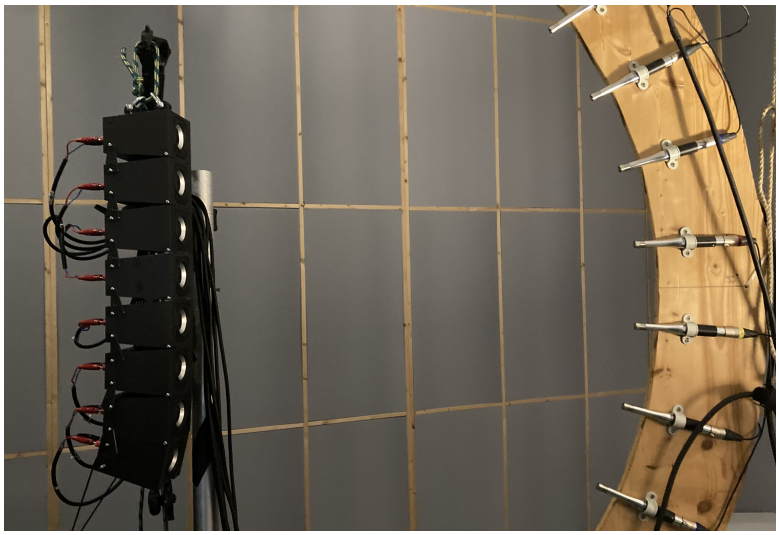

Figure 2.3: Experimental setup in configuration (1), with 0 dB per dod

$r_\mathrm{m} = 0.75\,\mathrm{m}$ from the origin. Fig. 2.3 shows the measurement environment during a measurement. The eight vertically arranged enclosures of height $h_\mathrm{ls} = 0.082\,\mathrm{m}$ are centered around the origin and mounted on a loudspeaker stand with a curved brace. The suspension was attached to an automatic rotation table to measure a full sphere around the array. A *Pure Data* patch performed all the measurements and controlled the rotating table. For the horizontal discretization, the same angle step of 10° was chosen, which resulted in 36 measurement runs. Having 18 zenith angles ϑ, 36 azimuth angles φ, and eight loudspeakers resulting in a total of $18 \times 36 \times 8 = 5184$ measured IRs. Fig. 2.4 sketches the dimensions of the experimental setup in LA-configuration (1) in a side and a top view. For simplification in mounting, the array tilt angle, indicated in table 2.1 was not realized in the

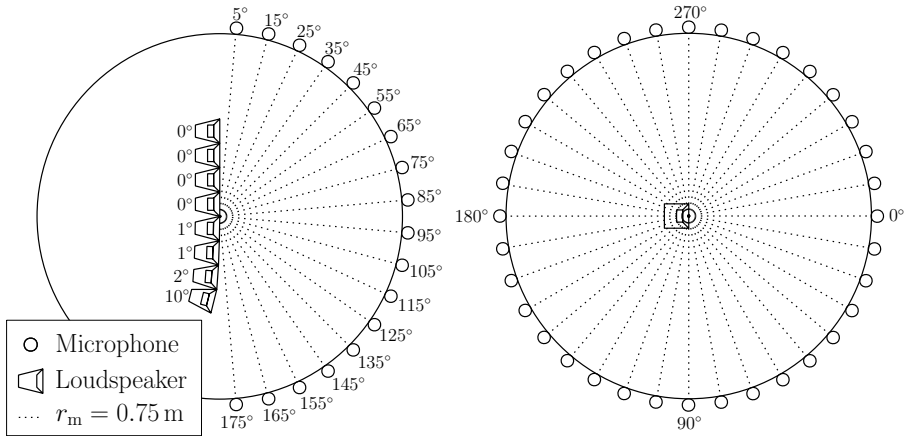

Figure 2.4: Sketch of the experimental setup in configuration (1). Left: side view. Right: top view

measured configuration. In hindsight, this angle was virtually applied by evaluating the polar pattern in section 2.3.3 by changing the microphone positions virtually by the array tilt angle.

2.2.1 Measurement Procedure

The *Pure Data* patch automatically played back the MES and recorded the microphone signals of all 18 microphones/zenith angles φ into a single 18-channel `.wav`-file. After a measuring pass, *Pure Data* controlled the rotation table and changed the azimuth angle by $\varphi = 10\,°$, then the next run was launched. After all 36 azimuth angles φ, the measurement of one LA configuration was finished.

2.3 Post-Processing

2.3.1 Calculation of the IRs (Sensitivity Correction and Direct Sound Equalization)

The sensitivity mismatch along the 18 microphones is compensated by recording the 1 kHz sine tone at 94 dB from the SPL calibration tool, the stationary part of each time signal is extracted, a FT is performed, and then the amplitude offset of each 1 kHz bin is obtained and corrected in the time domain. A *Python* script reads all the `.wav`-files from one configuration and performs a FT of all channels $x_{\varphi,\vartheta}[n]$ and of the inverse MES $x_{\text{inv}}[n]$ as

$$X_{\varphi,\vartheta}(e^{-\mathrm{i}\omega}) = \mathcal{F}\left\{x_{\varphi,\vartheta}[n]\right\} \qquad \text{and} \qquad X_{\text{inv}}(e^{-\mathrm{i}\omega}) = \mathcal{F}\left\{x_{\text{inv}}[n]\right\} . \tag{2.8}$$

As described in section 2.1, the deconvolution is applied in the frequency domain as

$$h_{\varphi,\vartheta}[n] = \mathfrak{Re}\left\{\mathcal{F}^{-1}\left\{\frac{X_{\varphi,\vartheta}(e^{-\mathrm{i}\omega}}{X_{\text{inv}}(e^{-\mathrm{i}\omega}}\right\}\right\} , \tag{2.9}$$

resulting in the IRs $h_{\varphi,\vartheta}[n]$, which include all IRs from the eight loudspeakers for a single microphone position. To obtain the single IRs for each loudspeaker microphone combination, the $h_{\varphi,\vartheta}[n]$ needs to be cut into eight single IRs with a length of $N = 1024$ samples, such that $h_{\varphi,\vartheta,\text{ls}}[n]$ comes up. Afterward, each microphone's calculated correction gain from section 2.3.1 is applied to the IRs. As known from [GZM23], all obtained IRs should be filtered with two peak filters, depicted in Fig. 2.5 to equalize the loudspeaker towards a flat direct sound frequency response.

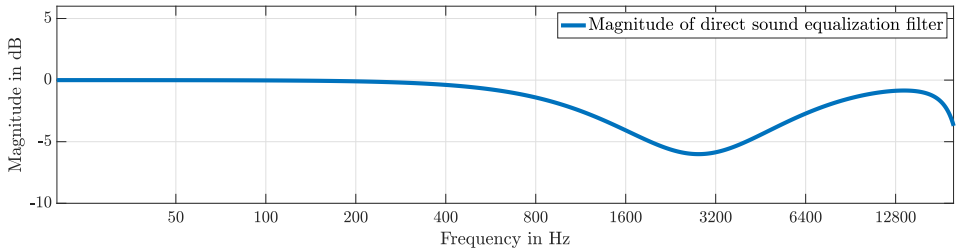

Figure 2.5: Filter: $f_1 = 2.8\,\text{kHz}, g_1 = -6\,\text{dB}, Q_1 = 0.8$ and $f_2 = 22\,\text{kHz}, g_2 = -10.5\,\text{dB}, Q_2 = 1.69$

2.3.2 Truncation

To avoid first reflections from the room during measurement, the IRs $h_{\varphi,\vartheta,\text{ls}}[n]$ are truncated to $N_{\text{cut}} = 185$ samples by finding the first prominent peak and then applying a tapered cosine window (turkey window) with a cosine factor of 0.09. The window is shifted by a transient time $t_{\text{transient}} = 20$ samples to include the transient process. An exemplary IR and the truncation window are shown in

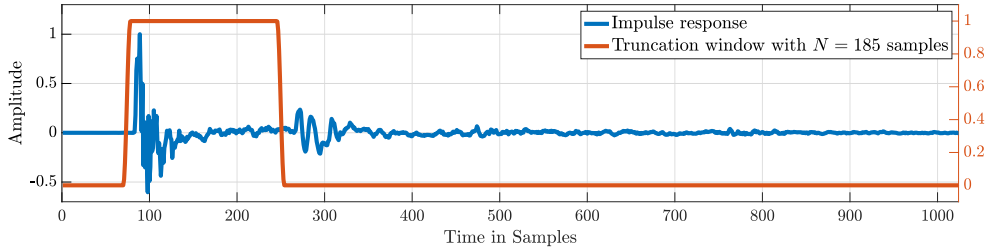

Figure 2.6: Exemplary truncation

Fig. 2.6. For further calculation, the truncated IR $h'_{\varphi,\vartheta,\text{ls}}[n]$ is Fourier transformed into the frequency domain, resulting in the complex transfer function

$$H_{\varphi,\vartheta,\text{ls}}(e^{-\mathrm{i}\omega}) = \mathcal{F}\left\{h'_{\varphi,\vartheta,\text{ls}}[n]\right\} . \tag{2.10}$$

2.3.3 Polar Pattern

The main focus of this report deals with the beamforming capability and line source directivity in vertical radiation orientation of the investigated LA. Therefore, only the polar pattern in this orientation is evaluated. Accordingly, the observation points of interest are the 18 measurements at $\varphi = 0\,^\circ$ and $\varphi = 180\,^\circ$, composed towards a circle of 36 microphone locations such

$$H_{\varphi,\vartheta,\mathrm{ls}}(e^{-\mathrm{i}\omega}) \qquad \longrightarrow \qquad H_{\mathrm{mic,ls}}(e^{-\mathrm{i}\omega}) \tag{2.11}$$

Phase and Amplitude Compensation

It is favorable for the interpolation performance at high frequencies to remove the complication of the amplitude and phase of an off-center source (see $r_{\mathrm{mic,ls}}$ in Fig. 2.7) from the polar pattern of every array loudspeaker. Fig. 2.7 shows an exemplary geometric sketch of these distances for the second loudspeaker for a single azimuth angle φ. Having the exact positions of all loudspeakers (x_{ls} and z_{ls}),

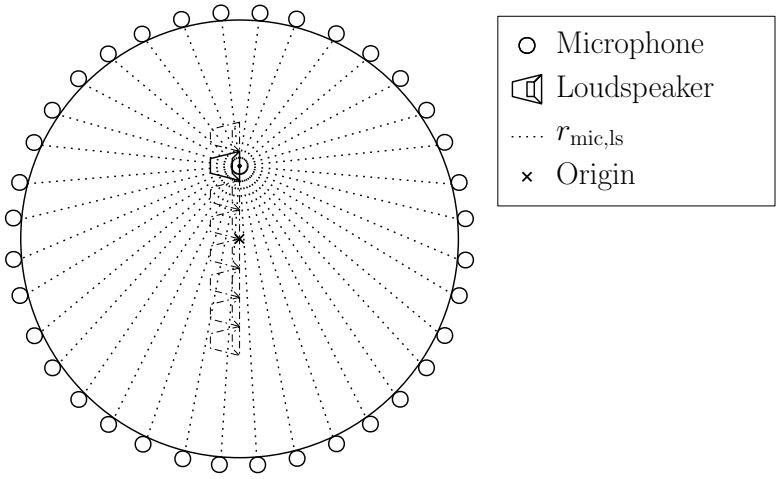

Figure 2.7: Unequal loudspeaker to microphone distances

the circular angles of the microphones from the origin $\vartheta_{\mathrm{mic,ls}}$ and the radius of the measured circle $r_{\mathrm{m}} = 0.75\,\mathrm{m}$, $r_{\mathrm{mic,ls}}$ is calculated with

$$r_{\mathrm{mic,ls}} = \sqrt{(r_{\mathrm{m}}\sin(\vartheta_{\mathrm{mic,ls}}) - x_{\mathrm{ls}})^2 + (r_{\mathrm{m}}\cos(\vartheta_{\mathrm{mic,ls}}) - z_{\mathrm{ls}})^2}\,. \tag{2.12}$$

Using Green's function in the frequency domain $G_{r_{\mathrm{mic,ls}}}(e^{-\mathrm{i}\omega})$

$$G_{r_{\mathrm{mic,ls}}}(e^{-\mathrm{i}\omega}) = \frac{e^{-\mathrm{i}kr_{\mathrm{mic,ls}}}}{4\pi r_{\mathrm{mic,ls}}} \qquad \text{with} \qquad k = \frac{\omega}{c}\,, \tag{2.13}$$

we compensate the level and phase offset by dividing the complex transfer function $H_{\mathrm{mic,ls}}(e^{-\mathrm{i}\omega})$ with $G_{r_{\mathrm{mic,ls}}}(e^{-\mathrm{i}\omega})$ for each loudspeaker microphone combination respectively, and express the microphone indices as zenith angles ϑ_{mic}, as

$$\hat{H}_{\mathrm{mic,ls}}(e^{-\mathrm{i}\omega}) = \frac{H_{\mathrm{mic,ls}}(e^{-\mathrm{i}\omega})}{G_{r_{\mathrm{mic,ls}}}(e^{-\mathrm{i}\omega})} = \hat{H}_{\vartheta_{\mathrm{mic}},\mathrm{ls}}(e^{-\mathrm{i}\omega}) \tag{2.14}$$

If the loudspeaker radiated omnidirectionally, this operation would cause a zero-phase, equal to $1/r$ amplitude at every microphone. For the non-omnidirectional case, the results display the deviations from the omnidirectional pattern observed at the relative locations between the loudspeaker and each microphone. This simplified phase-and-amplitude-compensated polar pattern is used for further calculations.

2D Interpolation of the simplified polar pattern

Circular harmonics (CH) are used to interpolate between the 10 ° discretized values of the amplitude-and-phase-simplified polar pattern to obtain a denser resolution of e.g. 1 °. Generally, the CHs for real x/z-coordinates, normalized with $\frac{1}{\sqrt{2\pi}}$ can be expressed with

$$Y^{(m)}(\vartheta) = \frac{1}{\sqrt{2\pi}} \begin{cases} \sqrt{2}\sin(|m|\,\vartheta) & \text{for } m = -1, ..., -M \\ 1 & \text{for } m = 0 \\ \sqrt{2}\cos(m\,\vartheta) & \text{for } m = 1, ..., M \end{cases}, \tag{2.15}$$

and in matrix notation with q as index for the number of Q angles

$$\mathbf{Y}_\vartheta = \underbrace{\left[\begin{array}{ccccccccc} \frac{\sin(M\vartheta_0)}{\sqrt{\pi}} & \frac{\sin((M-1)\vartheta_0)}{\sqrt{\pi}} & \cdots & \frac{\sin(\vartheta_0)}{\sqrt{\pi}} & \frac{1}{\sqrt{2\pi}} & \frac{\cos(\vartheta_0)}{\sqrt{\pi}} & \cdots & \frac{\cos((M-1)\vartheta_0)}{\sqrt{\pi}} & \frac{\cos((M)\vartheta_0)}{\sqrt{\pi}} \\ \frac{\sin(M\vartheta_1)}{\sqrt{\pi}} & \frac{\sin((M-1)\vartheta_1)}{\sqrt{\pi}} & \cdots & \frac{\sin(\vartheta_1)}{\sqrt{\pi}} & \frac{1}{\sqrt{2\pi}} & \frac{\cos(\vartheta_1)}{\sqrt{\pi}} & \cdots & \frac{\cos((M-1)\vartheta_1)}{\sqrt{\pi}} & \frac{\cos((M)\vartheta_1)}{\sqrt{\pi}} \\ \vdots & \vdots & \vdots & \vdots & \vdots & \vdots & \vdots & \vdots & \vdots \\ \frac{\sin(M\vartheta_q)}{\sqrt{\pi}} & \frac{\sin((M-1)\vartheta_q)}{\sqrt{\pi}} & \cdots & \frac{\sin(\vartheta_q)}{\sqrt{\pi}} & \frac{1}{\sqrt{2\pi}} & \frac{\cos(\vartheta_q)}{\sqrt{\pi}} & \cdots & \frac{\cos((M-1)\vartheta_q)}{\sqrt{\pi}} & \frac{\cos((M)\vartheta_q)}{\sqrt{\pi}} \end{array}\right]}_{2M+1} \Bigg\} Q \tag{2.16}$$

Using $\mathbf{Y}_{\vartheta_\mathrm{mic}}$ and $\mathbf{Y}_{\tilde{\vartheta}}$, where ϑ_mic are the measured angles and $\tilde{\vartheta}$ the new angles for interpolation, we can calculate the dense mesh of interpolated points from the sparse mesh of measured points with

$$\tilde{H}_{\tilde{\vartheta},ls}(e^{-\mathrm{i}\omega}) = \mathbf{Y}_{\tilde{\vartheta}}\,(\mathbf{Y}^{-1}_{\vartheta_\mathrm{mic}}\,\hat{H}_{\vartheta_\mathrm{mic},\mathrm{ls}}(e^{-\mathrm{i}\omega}))^T \tag{2.17}$$

The number of measured angles in the vertical plane is $Q = 36$. We can choose a denser interpolation grid with several angles of $\tilde{Q}$. For this purpose, an interpolation grid with $\tilde{Q} = 360$ angles with a harmonic order $M = 17$ was used. Increasing the spatial discretization is mandatory to evaluate the decay behavior in the far field.

2.3.4 Extrapolation to the Far Field

In addition to the polar pattern for a given distance, the decay behavior with increasing distance is the subject of this report. Generally, the measured and interpolated vertical polar pattern at the evaluated azimuth orientation, $\tilde{H}_{\tilde{\vartheta},\mathrm{ls}}(e^{-\mathrm{i}\omega})$ is evaluated at angles $\tilde{\vartheta} = \vartheta_x$, which aim at observation points on a virtual listener distance to obtain the sound pressure at these directions. Fig. 2.8 shows the desired geometry of listeners distance from 0 m to 10 m, where the array tilt angle is already applied as indicated by the rotated microphone positions. Adding the characteristic level drop and

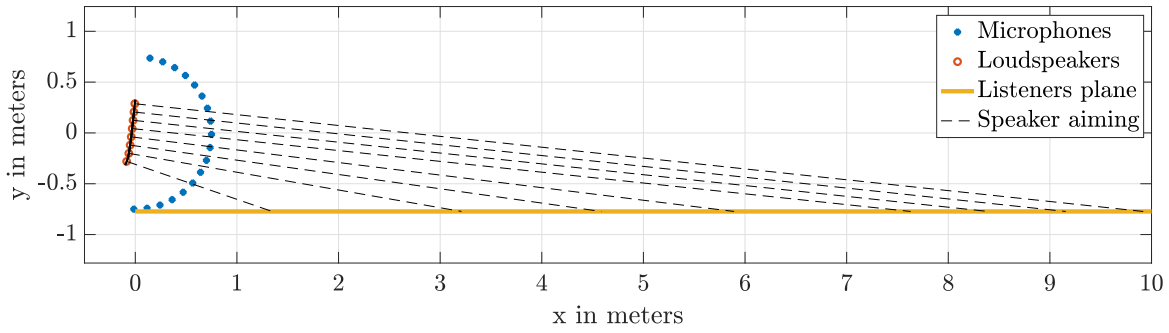

Figure 2.8: Sketch of the geometry for the far field extrapolation in configuration (1).

phase shift, defined by Green's function $G_{r_{\mathrm{ls},x}}(e^{-\mathrm{i}\omega})$, for each loudspeaker-observation-point distance

$r_{\mathrm{ls},x} = \sqrt{\tilde{x}_{\mathrm{fl}}^2 + \tilde{z}_{\mathrm{ls}}^2}$ (see Fig. 2.10 for dimensions), the complex transfer function $H_{\mathrm{ls},x}(e^{-\mathrm{i}\omega})$ is given at these points for each loudspeaker. Adding up all eight $H_{\mathrm{ls},x}(e^{-\mathrm{i}\omega})$ for each point result in $H_x(e^{-\mathrm{i}\omega})$ as

$$H_x(e^{-\mathrm{i}\omega}) = \sum_{\mathrm{ls}} H_{\mathrm{ls},x}(e^{-\mathrm{i}\omega}) = \sum_{\mathrm{ls}} \tilde{H}_{\vartheta_x,\mathrm{ls}}(e^{-\mathrm{i}\omega})\, G_{r_{\mathrm{ls},x}}(e^{-\mathrm{i}\omega})\,. \tag{2.18}$$

Parallax angles

Having virtually moved the speakers to the origin in the 2.3.3 section, there is an angular mismatch between the observation points and the original position of the speakers. The correct evaluation angle of one loudspeaker-observation-point combination ϑ_x must be adapted to a parallax angle $\tilde{\vartheta}_x$, which is the correct mapping for the original layout. Evaluating the polar pattern at this parallax angle $\tilde{\vartheta}_x$ leads to the correct pressure values at the point of impact on the measured sphere. Having the origin point at $x_0 = 0\,\mathrm{m}$ with $z_0 = z_{\mathrm{top}} - 4\,h_{\mathrm{ls}} = 1.06\,\mathrm{m} - 0.328\,\mathrm{m} = 0.732\,\mathrm{m}$ and the probe location at zero height at x_{fl}, the angle to that impact point ϑ_x is defined as

$$\vartheta_x = \tan^{-1}\left(\frac{x_{\mathrm{fl}}}{z_{\mathrm{ls}}}\right) \qquad \text{with} \qquad z_{\mathrm{ls}} = z_0 - z_1\,, \tag{2.19}$$

where z_1 is known from the experimental setup. Fig. 2.9 shows an exemplary sketch of the geometric context. Expressing x_{m} as the sinusoidal relation of the angles ϑ_x and $\tilde{\vartheta}_x$, the distance from a

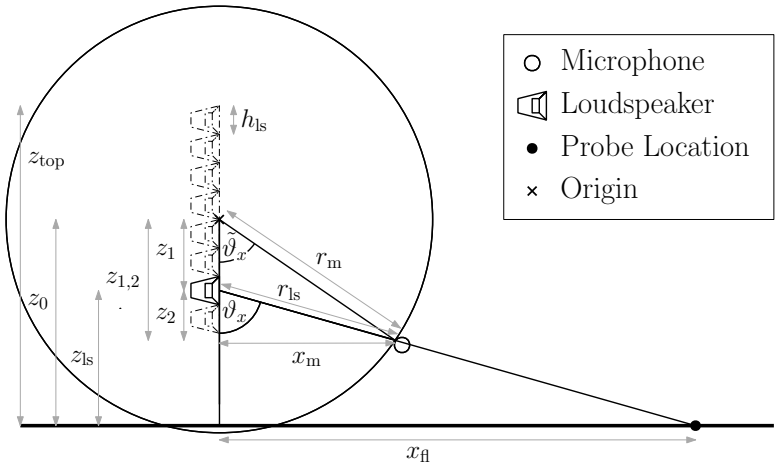

Figure 2.9: Parallax angles

loudspeaker to the microphone, r_{ls} is given by

$$x_{\mathrm{m}} = r_{\mathrm{ls}} \sin(\vartheta_x) = r_{\mathrm{m}} \sin(\tilde{\vartheta}_x) \quad \Rightarrow \quad r_{\mathrm{ls}} = r_{\mathrm{m}}\, \frac{\sin(\tilde{\vartheta}_x)}{\sin(\vartheta_x)}\,. \tag{2.20}$$

Defining z_2 with

$$z_2 = r_{\mathrm{ls}} \cos(\vartheta_x) = r_{\mathrm{m}}\, \frac{\sin(\tilde{\vartheta}_x)}{\sin(\vartheta_x)} \cos(\vartheta_x) \tag{2.21}$$

leads to the equation

$$z_{1,2} = z_1 + z_2 = r_{\mathrm{m}} \cos(\tilde{\vartheta}_x) = z_1 + r_{\mathrm{m}}\, \frac{\sin(\tilde{\vartheta}_x)}{\sin(\vartheta_x)} \cos(\vartheta_x) \quad \Rightarrow \quad z_1 = r_{\mathrm{m}} \left(\cos(\tilde{\vartheta}_x) - \frac{\sin(\tilde{\vartheta}_x)}{\sin(\vartheta_x)} \cos(\vartheta_x) \right), \tag{2.22}$$

where the wanted parallax angle $\tilde{\vartheta}_x$ is the only unknown. After rewriting eq. (2.22) to

$$\frac{z_1}{r_{\mathrm{m}}} \sin(\vartheta_x) = \cos(\tilde{\vartheta}_x) \sin(\vartheta_x) - \sin(\tilde{\vartheta}_x) \cos(\vartheta_x)\,, \tag{2.23}$$

the trigonometric theorem

$$\cos(A)\sin(B) - \sin(A)\cos(B) = \sin(B - A)\,, \tag{2.24}$$

is used to simplify eq. (2.23) to

$$\frac{z_1}{r_\mathrm{m}}\sin(\vartheta_x) = \sin(\vartheta_x - \tilde{\vartheta}_x)\,. \tag{2.25}$$

Due to the tilt of the overall array and successively angled loudspeakers, x_fl and z_1 need to be corrected by $\tilde{x}_\mathrm{fl} = x_\mathrm{fl} + \tilde{x}$ and $\tilde{z}_1 = z_1 - \tilde{z}$. The dimensions are sketched exemplarily in Fig. 2.10, such that the final parallax angle can be obtained by rewriting Eq. (2.25) to

$$\tilde{\vartheta}_x = \vartheta_x - \sin^{-1}\left(\frac{\tilde{z}_1}{r_\mathrm{m}}\sin(\vartheta_x)\right)\,, \qquad \text{where} \qquad \vartheta_x = \tan^{-1}\left(\frac{\tilde{x}_\mathrm{fl}}{\tilde{z}_\mathrm{ls}}\right). \tag{2.26}$$

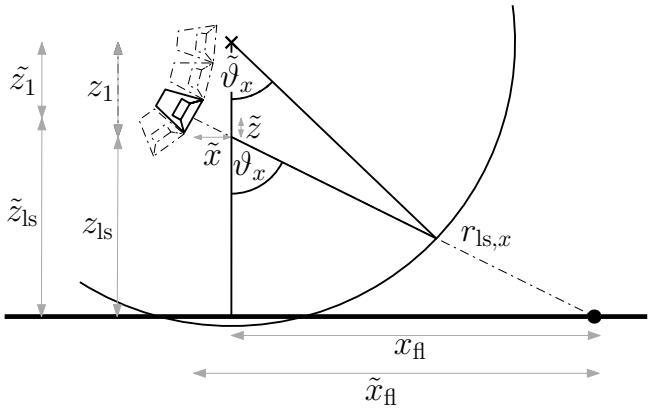

Figure 2.10: Offset for parallax angles

2.3.5 LA equalization, broadband A-weighting and third-octave filters

After calculating $H_x(e^{-\mathrm{i}\omega})$ at each observation point with the adapted parallax angle $\tilde{\vartheta}_x$, some further filtering is required. To match human perception, an A-Weighing filter was used, whose transfer function[1] is given as

$$H_\mathrm{A}(\mathrm{i}\omega) = \frac{k_\mathrm{A}(\mathrm{i}\,\omega)^4}{((\mathrm{i}\,\omega)+129.4)^2((\mathrm{i}\,\omega)+676.7)((\mathrm{i}\,\omega)+4636)((\mathrm{i}\,\omega)+76617)^2}\,, \qquad \text{with} \qquad k_\mathrm{A} = 7.39705{\times}10^9\,. \tag{2.27}$$

The magnitude of the A-Weigthing filter is shown in Fig. 2.11. $H_x(e^{-\mathrm{i}\omega})$ is filtered with $H_\mathrm{A}(\mathrm{i}\omega)$ in

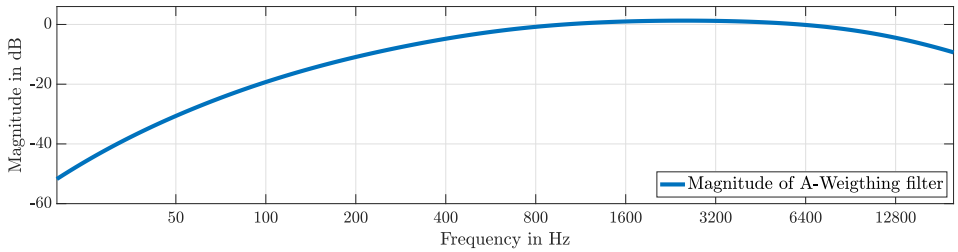

Figure 2.11: Magnitude of A-Weigthing filter

[1] https://en.wikipedia.org/wiki/A-weighting

the complex domain as

$$H_{x,\mathrm{A}}(e^{-\mathrm{i}\omega}) = H_x(e^{-\mathrm{i}\omega})\, H_\mathrm{A}(\mathrm{i}\omega)\,. \tag{2.28}$$

Since the LA shows a spectral pink noise behavior, a correction filter (CF) $|H_\mathrm{CF}(e^{-\mathrm{i}\omega})|$ (shown in Fig. 2.12) compensates the summed frequency response up to the spatial aliasing frequency ω_aliasing and reads as

$$|H_\mathrm{CF}(e^{-\mathrm{i}\omega})| = \min\left(\sqrt{\frac{\omega}{\omega_\mathrm{aliasing}}}, 1\right)\,. \tag{2.29}$$

The spatial aliasing frequency $\omega_\mathrm{aliasing} = \frac{2\,\pi\,c}{d_\mathrm{ls}}$ is defined by the centrical distance of neighboring chassis $d_\mathrm{ls} = 0.082\,\mathrm{m}$. This filter is applied to $H_{x,\mathrm{A}}(e^{-\mathrm{i}\omega})$ in the absolute domain as

$$H_{x,\mathrm{A,CF}}(\omega) = |H_\mathrm{CF}(e^{-\mathrm{i}\omega})|\,|H_{x,\mathrm{A}}(e^{-\mathrm{i}\omega})|\,. \tag{2.30}$$

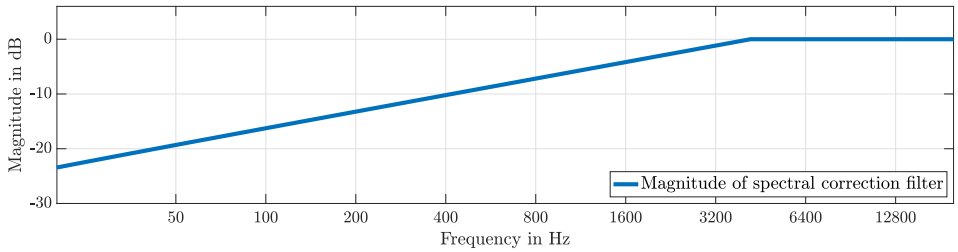

Figure 2.12: Spectral correction Filter with $f_\mathrm{aliasing} = 4146.34\,\mathrm{Hz}$

The average (RMS) relative sound pressure level (SPL) in decibels over the entire frequency range at each observation point x is then calculated with

$$L_{A,\mathrm{RMS}}(x) = 20\,\log_{10}\left(\sqrt{\frac{1}{N}\sum_{\omega=0}^{N}|H_{x,\mathrm{A,CF}}(\omega)|^2}\right) \qquad \text{where} \qquad N = \frac{fs}{2} - 1\,. \tag{2.31}$$

To investigate the frequency-dependent decay, $H_{x,\mathrm{A,CF}}(\omega)$ was smoothed to third-octave bands using a $\cos^2$ filter bank with magnitudes shown in Fig. 2.13.

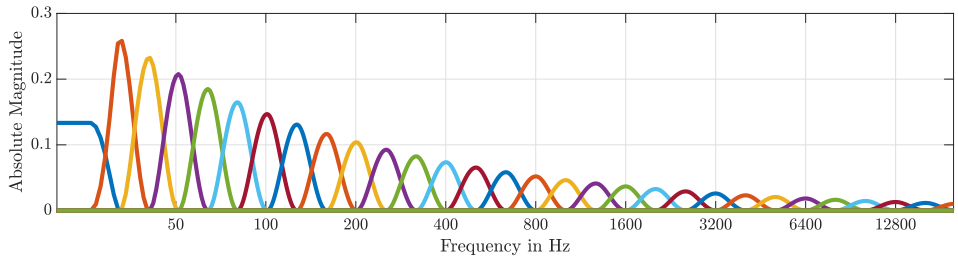

Figure 2.13: Magnitudes of $\cos^2$ third-octave filters

3 Results

3.1 Polar Pattern

This report investigated only the vertical directivity of the different configurations with azimuth angle $\varphi = 0\,^\circ$. Due to the CH decomposition and evaluation using parallax angles, it is possible to obtain representations of the polar patterns at different distances. The typical radius of 1 m was used to compare different configurations. The angular representation is the same as in Fig. 2.4 in section 2.2, where $0\,^\circ$ corresponds to upward radiation, $90\,^\circ$ represents the main direction, $180\,^\circ$ corresponds to downward radiation and the $270\,^\circ$ represents backwards radiation of the loudspeaker.

Single Speaker

The fourth loudspeaker in configuration (4) is closest to the origin and is a point source reference for further investigations. In Fig. 3.1 the polar pattern at $f = [800\,\text{Hz}, 2500\,\text{Hz}, 4000\,\text{Hz}]$ of this single speaker is depicted for a radius $r_m = 1\,\text{m}$. At 800 Hz, the polar pattern is almost omnidirectional with

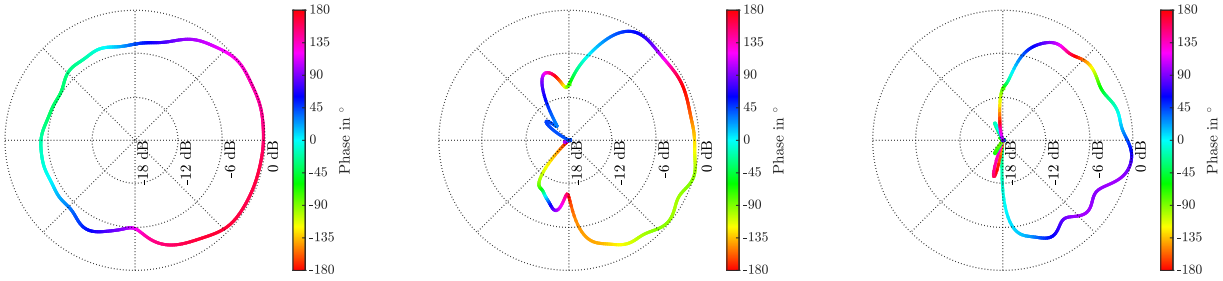

800 Hz 2.5 kHz 4 kHz

Figure 3.1: Single speaker at 1 m

rear damping of $-6\,\text{dB}$. The directivity increases by raising the observed frequency due to a relatively larger membrane diameter. In the theory of piston radiators in infinitely large surfaces, the directivity angle at $f = 4\,\text{kHz}$ for a diaphragm radius of $r_d = 3.175\,\text{cm}$ is defined with

$$\phi(f = 4\,\text{kHz}) = 2\sin^{-1}\left(\frac{2.22}{k\,r_d}\right) \approx 145\,^\circ \qquad \text{with} \qquad k = \frac{2\pi f}{c}\,, \tag{3.1}$$

which almost matches the polar pattern of the single loudspeaker in Fig. 3.1 at 4 kHz.

Configuration 1

The polar pattern in 1 m distance of configuration 1 in Fig. 3.2 shows a drastic increase in directivity at all evaluated frequencies compared to the single loudspeaker. At 800 Hz, the polar pattern already shows a significant beamforming towards the front and back. The rear damping of $-6\,\text{dB}$ corresponds with the damping of the single speaker. A dispersion angle of around $40\,^\circ$ at 2.5 kHz indicates the operation principle of a line source. Above the spatial aliasing frequency $f_{\text{aliasing}} = \frac{c}{d_{\text{ls}}} = 4146.34\,\text{Hz}$ the relatively large inter-chassis distances compared to the wavelength causes an interference pattern along the line source in the vertical domain. A constructive interference is observable above and

below the LA at the spatial aliasing frequency. The frontal dispersion angle of 30 ° at 4 kHz can be determined at the −6 dB limits of the polar plot. The length of the LA defines the lower frequency

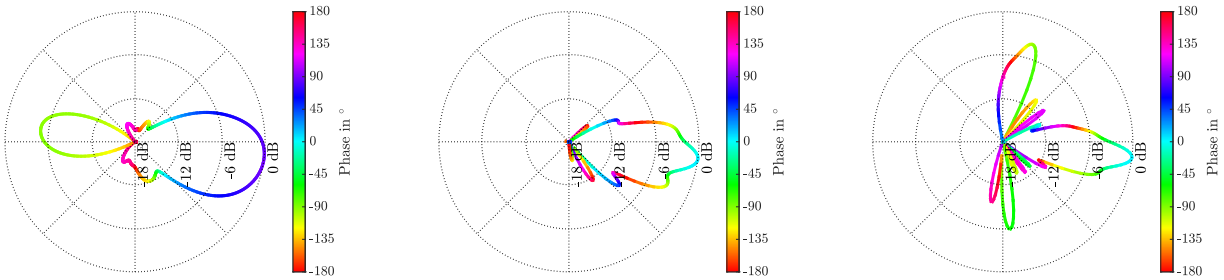

800 Hz 2.5 kHz 4 kHz

Figure 3.2: Configuration 1 at 1 m

limit to operate as a line source. To investigate this boundary, Fig. 3.3 displays the polar pattern for the frequencies [100 Hz, 200 Hz, 400 Hz]. The LA shows an almost omnidirectional radiation behavior at 100 Hz. A tiny beamforming effect with −3 dB side and rear damping is visible at 200 Hz. The polar plot at 400 Hz shows already a side damping of −12 dB for which we can presume that the LA begins to act as a line source. From theory, we know that the lower-frequency bound f_{low} for line

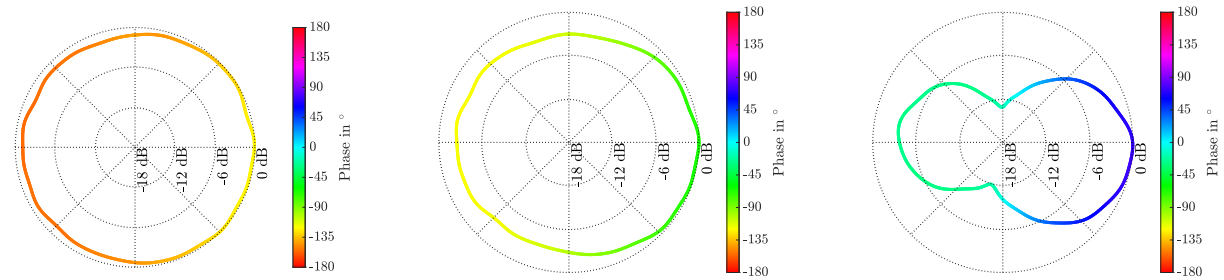

100 Hz 200 Hz 400 Hz

Figure 3.3: Configuration 1 at 1 m

source behavior is dependent on the total array length $l_{\text{LA}} = 65.6\,\text{cm}$. The LA starts acting as a line source as the radiated wavelength reaches the dimension of the array length, so in our case, the lower bound is $f_{\text{low}} \approx \frac{c}{l_{\text{LA}}} \approx 500\,\text{Hz}$. Applications for line source arrays are typically in the long throw. The

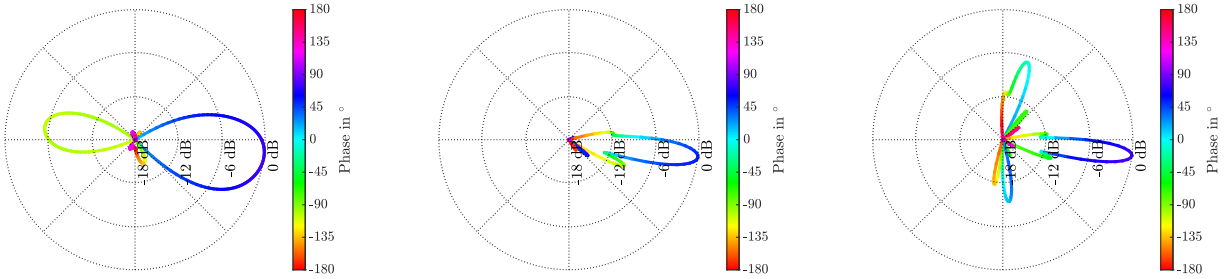

800 Hz 2.5 kHz 4 kHz

Figure 3.4: Configuration 1 at 4 m

polar pattern is extrapolated to a radius of 4 m for the three evaluated frequency bands in Fig. 3.4 to

illustrate the beamforming capability of this array. Especially at 2.5 kHz, the polar pattern indicates proper beamforming towards the listener area, having a dispersion angle of $< 20\,^\circ$. It shows that even at this distance, the spatial aliasing lobes at 4 kHz are that dominant.

Configuration 2

The second investigated design in configuration 2 aims for a decay of -1.5 dB per dod. Fig. 3.5 displays the polar pattern at the three frequencies of interest. Overall, the polar pattern at the frequencies of interest is very similar to configuration 1. A slight increase of level towards the 115 ° direction (especially at 2.5 kHz) is observable and can be explained by the curvature of this configuration. At 4 kHz, the spatial aliasing equals the one of configuration 1, but the main lobe in the 95 ° direction seems slightly more comprehensive.

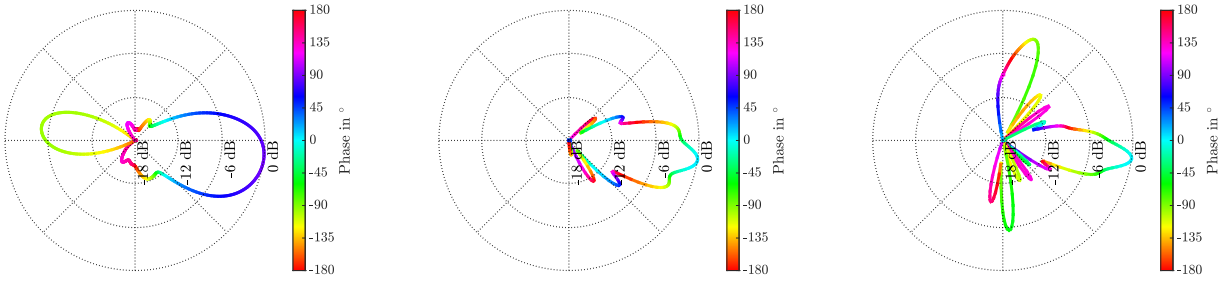

800 Hz 2.5 kHz 4 kHz

Figure 3.5: Configuration 2 at 1 m

Configuration 3

On the view of configuration 3 in Fig. 3.6, the differences between all three configurations are very gentle in the near field at 1 m. Only the spatial aliasing sidelobe is of a negligible different shape, and the main lobe is again slightly broader. Even at 800 Hz, the main lobe is more tilted downwards,

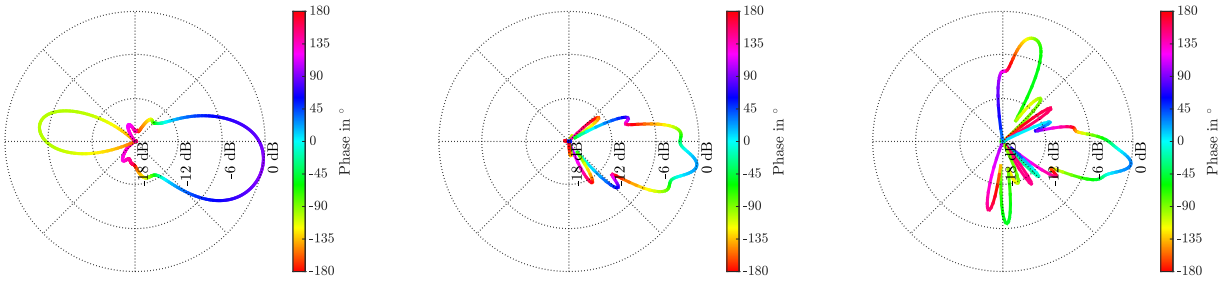

800 Hz 2.5 kHz 4 kHz

Figure 3.6: Configuration 3 at 1 m

indicating more sound pressure in the near field and a faster decay towards the far field. The three configurations' polar pattern is only meaningful in the near field. The extrapolation onto a one-dimensional listener depth seems reasonable, and the results are presented in the next section 3.2.

3.2 Decay

Using the presented methods in section2, the pressure measured points at the initial 10 ° grid are interpolated to a dense grid of 1 ° resolution and then extrapolated to a listener depth of 0 m − 16 m using the parallax angles. In the following figures, the depth (x-axis) is implemented as semi-logarithmic (linear from 0 m to 1 m, and then logarithmic) to simplify the observation of doubling the distance. Fig. 3.7 shows the A-weighted SPL decay of the single uppermost loudspeaker. The thin coloured lines are 1/3-octave bands with center frequencies [250 Hz, 500 Hz, 1000 Hz, 2000 Hz, 4000 Hz, 8000 Hz, 16 000 Hz]. The expected point source decay of −6 dB per dod is visible starting at a distance of 2 m. Due to the

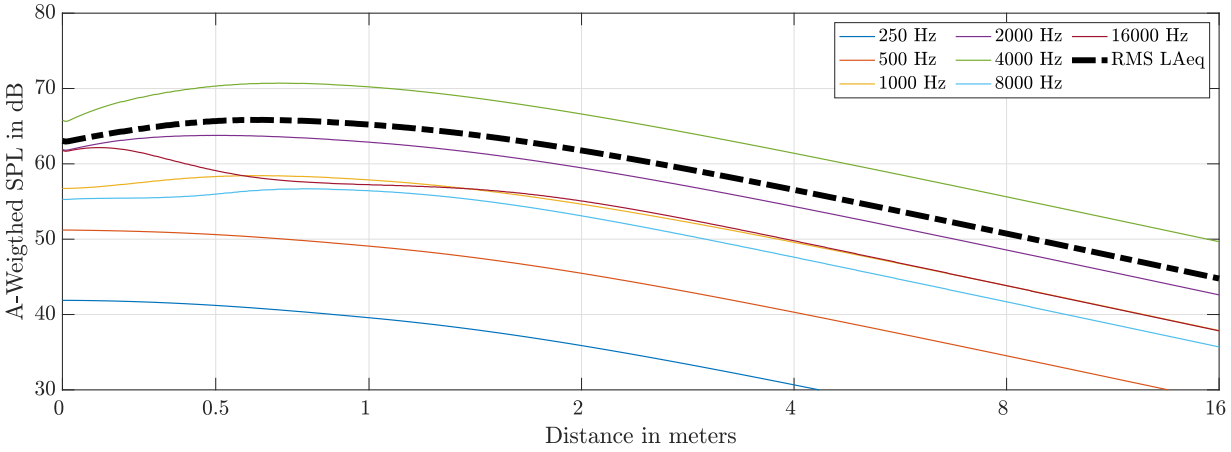

Figure 3.7: A-weighted SPL decay of a single speaker (uppermost)

directivity of the chassis at higher frequencies, the SPL under the loudspeaker at 0 m is less, and the $\frac{1}{r}$ decay behavior initially starts at 2 m. In contrast to the single loudspeaker, Fig. 3.8 depicts the decay of the LA in configuration 1. The blue dotted line illustrates the predicted design with 0 dB per dod from 1 m to 6 m. Beyond 6 m the SPL is expected to drop with −6 dB per dod. The A-weighted SPL

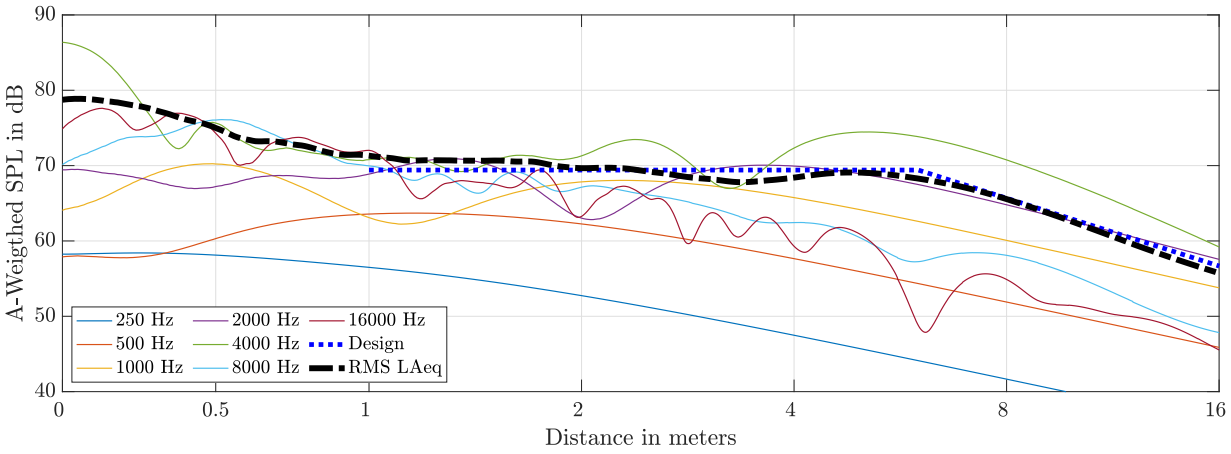

Figure 3.8: A-weighted SPL decay of configuration 1

of configuration 1 matches almost the design with minor deviations at 1 m and 3.5 m. Due to the 1 ° loudspeaker curvature angle resolution, the tiny mismatch of the design at 3.5 m occurs because the design could not be suspended accurately. Looking at the 1/3-octave bands, the spatial aliasing above 4 kHz and point source behavior below 500 Hz is observable. Especially in the range from 1 kHz to 4 kHz, the decay of 0 dB per dod is achieved.

The second configuration aims for a design with a decay of −1.5 dB per dod. Compared to the other designs, in configuration 2 the A-weighted SPL best matches the design slope as shown in Fig. 3.9. As observed earlier in the configuration, the frequencies between 1 kHz to 4 kHz show the best beamforming behavior, resulting in the most consistent decay. Spatial aliasing from the 4 kHz is also clearly visible.

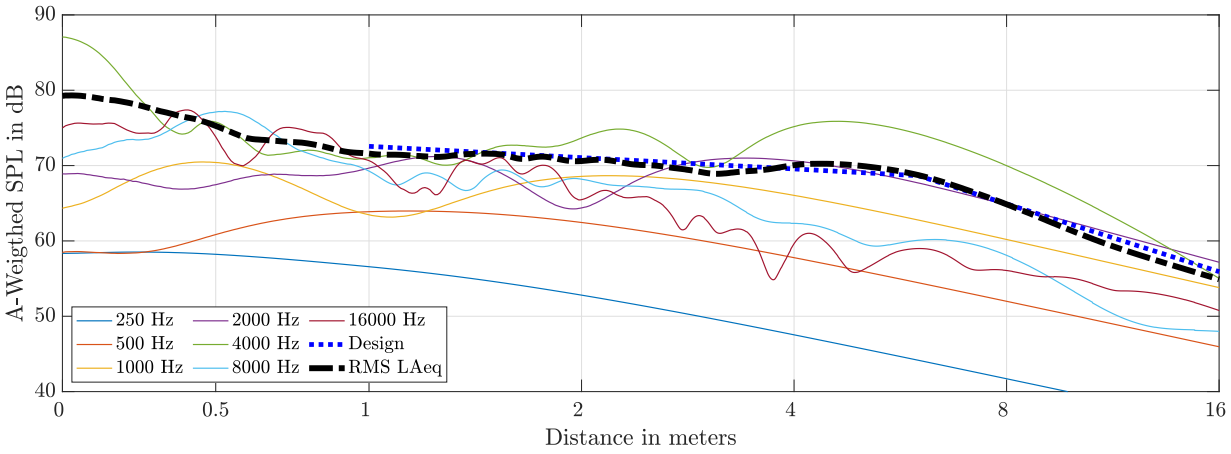

Figure 3.9: A-weighted SPL decay of configuration 2

The decay of configuration 3 is depicted in Fig. 3.10. The design of −3 dB is only partially achieved. Only in the tiny range from 2 m to 3 m the goal was reached. Between the distance of 1 m to 2 m, the SPL is significantly too low, while the one from 3 m is to high. The overall slope is more similar to a design of 0 dB per dod.

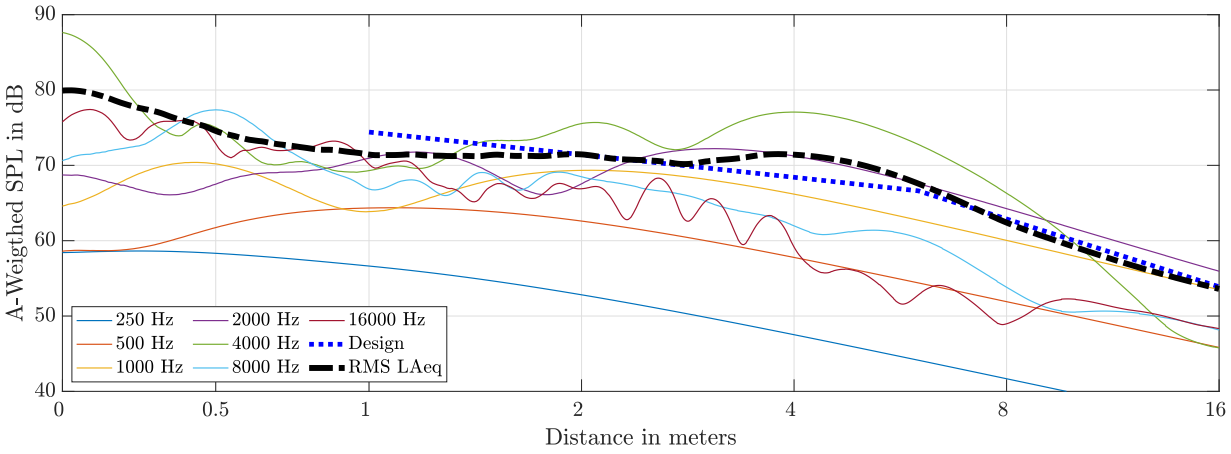

Figure 3.10: A-weighted SPL decay of configuration 3

4 Discussion & Conclusion

4.1 Discussion

In this report, measurements of a small-size variable curved line source array are processed and evaluated to gain knowledge about the circular radiation pattern in the near field and the decay behavior in the far field. Therefore, the geometric properties are studied in detail, and CH interpolations and extrapolations into the far field using parallax angles are performed to obtain valid results.

The resulting polar pattern confirms the results' validity and shows how the dispersion of the whole LA behaves in the near field. The radiation boundaries towards lower frequencies match the theory, and even spatial aliasing becomes visible. The extrapolation to larger radii illustrates a LA's beamforming effect but is unsuitable to predict the decay behavior in the far field.

Considering the angular displacement, evaluating parallax angles with subsequent extrapolation into the far field results in meaningful decay predictions. Due to limitations in precise curvature angle between the single loudspeaker, not all intended decays are achieved accurately.

4.2 Conclusion

In this report, the results of a measured loudspeaker array, which has only a coarse grid of microphones in a small near-field radius, are significantly improved using the methods presented. Interpolation using CH increases the angular resolution, mandatory for accurate evaluation at the displaced parallax angles. The listener depth can be precisely sampled by summing the individual loudspeaker impacts at one observation point, evaluated at the correct angle, and extended by the correct amplitude and phase supplement using the Greens function. This allows meaningful predictions of the far-field behavior of an array measured in the near-field. Compared to standard software applications, which superimpose the polar pattern of single enclosures, this technique even allows reflection and diffraction effects at the edges of neighboring loudspeakers.

Bibliography

[GZM23] L. Gölles, F. Zotter, and L. Merkel, "Miniature line array for immersive sound reinforcement," in *Audio Engineering Society Conference: AES 2023 International Conference on Spatial and Immersive Audio*, Aug 2023. [Online]. Available: http://www.aes.org/e-lib/browse.cfm?elib=22156

[HCZ09] M. Holters, T. Corbach, and U. Zölzer, "Impulse response measurement techniques and their applicability in the real world," in *Proceedings of the 12th International Conference on Digital Audio Effects, DAFx 2009*, 2009.

[MBL07] P. Majdak, P. Balazs, and B. Laback, "Multiple exponential sweep method for fast measurement of head-related transfer functions," *Journal of the Audio Engineering Society*, vol. 55, pp. 623–637, 07 2007.

[ZG22] F. Zotter and L. Gölles, "Exponentially swept sinusoid with zero-crossing in its beginning and end," https://git.iem.at/zotter/IR-Measurement-JupyterNotebook/-/blob/master/01-generate-zero-crossing-sweep.ipynb, 2022, online; accessed 14-12-2023.